Nanoscale



PAPER View Article Online
View Journal | View Issue



Cite this: Nanoscale, 2021, 13, 14408

Structure evolution and energy storage mechanism of Zn₃V₃O₈ spinel in aqueous zinc batteries†

Haocong Yi,‡ Changjian Zuo,‡ Hengyu Ren, Wenguang Zhao, Yuetao Wang, Shouxiang Ding, Yang Li, Runzhi Qin,

\begin{align} \text{ \text{ Lin Zhou, Lu Yao, Shunning Li, } \\ \text{ Qinghe Zhao* and Feng Pan } \text{ \text{ \text{ P}} * Lin Zhou, Lu Yao, Shunning Li, } \\ \text{ \text{ Lin Zhou, Lu Yao, Shunning Li, } \\ \text{ \text{ Lin Zhou, Lu Yao, Shunning Li, } \\ \text{ Lin Zhou, Lu Yao, Shunning Li, } \\ \text{ Lin Zhou, Lu Yao, Shunning Li, } \\ \text{ Lin Zhou, Lu Yao, Shunning Li, } \\ \text{ Lin Zhou, Lu Yao, Shunning Li, } \\ \text{ Lin Zhou, } \\ \text{ Lin Zhou, Lu Yao, Shunning Li, } \\ \text{ Lin Zhou, } \\ \text{ Lin Zhou, Lu Yao, Shunning Li, } \\ \text{ Lin Zhou, } \\ \text{ Lin Zhou, Lu Yao, Shunning Li, } \\ \text{ Lin Zhou, } \\ \text{ L

Spinel-type materials are promising for the cathodes in rechargeable aqueous zinc batteries. Herein, $Zn_3V_3O_8$ is synthesized *via* a simple solid-state reaction method. By tuning the $Zn(CF_3SO_3)_2$ concentration in electrolytes and the cell voltage ranges, improved electrochemical performance of $Zn_3V_3O_8$ can be achieved. The optimized test conditions give rise to progressive structure evolution from bulk to nanocrystalline spinel, which leads to capacity activation in the first few cycles and stable cycling performance afterward. Furthermore, the energy storage mechanism in this nano-crystalline spinel is interpreted as the co-intercalation of zinc ions and protons with some water. This work provides a new viewpoint of the structure evolution and correlated energy storage mechanism in spinel-type host materials, which would benefit the design and development of next-generation batteries.

Received 14th April 2021, Accepted 9th July 2021 DOI: 10.1039/d1nr02347k

rsc.li/nanoscale

Introduction

As one of the most promising next-generation batteries, the rechargeable aqueous zinc-ion battery (AZIB) with mild acid electrolytes has recently attracted much attention, mainly due to the low cost, high ionic conductivity, and high safety of the aqueous electrolytes. 1-4 Seeking a suitable cathode material is significant for the practical application of AZIBs. Nowadays, the electrode performances of several cathode materials have been intensively investigated in aqueous batteries, including vanadium oxides,^{5,6} manganese oxides,^{7,8} Prussian blue analogues, 9,10 organic species, 11,12 etc. Although they exhibit excellent electrode performances, their synthesis methods might be too complex for mass-production, and the undesirable cost may be a crucial factor for the application of ZIBs. In this sense, more research needs to be done to select high-performance cathode materials synthesized via facile solid-state synthesis, which is a general mass-production method in the industry. 13-15

Spinel-type crystals, such as $ZnMn_2O_4$, 16,17 ZnV_2O_4 , 18 MgV_2O_4 , 19 etc., have high research value. Solid-state reactions

School of Advanced Materials, Peking University Shenzhen Graduate School, Shenzhen 518055, China. E-mail: bushihaoren@pku.edu.cn, zhaoqh@pku.edu.cn, panfeng@pkusz.edu.cn which suit the requirement of mass production can be applied. However, compared with pure metal oxides, the spinel-type materials usually suffer from low capacity delivery due to the relatively low valence of transition metal ions, as well as the limited ion diffusion kinetics in dense face-centered cubic lattices. Thus, recent research studies on spinel-type cathodes mainly highlight the optimization strategies to enhance the capacity delivery, including defect engineering, tuning electronic/coordination environments, structure evolution, *etc.* The cation-defective ZnMn₂O₄¹⁷ and the *in situ* oriented Mn deficient ZnMn₂O₄@C¹⁶ were reported to achieve high capacity delivery in aqueous Zn-ion batteries, in which the defect engineering opens up additional pathways for easier migration of more carrier ions.

The environments of TM–O coordination (TM represents transition metal ions) in spinel are usually modulated *via* metal doping. For example, Ji *et al.*²² reported that regulating the electronic state of Mn–O *via* Co₂^{+/3+/4+} doping in Mn₃O₄ plays a role in promoting ion diffusion and inhibiting the Jahn–Teller effect in discharge products. Pan *et al.*²³ reported that Ni and Mn doping in ZnCo₂O₄ spinel can stabilize the spinel structure during Zn²⁺ insertion/extraction processes, and multiple conversions of Mn⁴⁺/Mn³⁺, Ni⁴⁺/Ni³⁺/Ni²⁺ and Co⁴⁺/Co³⁺ are responsible for the enhanced capacity. Besides, Zuo *et al.*²⁴ revealed that the Li/Mn disorder in LiMn₂O₄ spinel can prevent the Mn³⁺–O bonds from distorting along one direction, which enhances the structural stability and activates more electrochemically active sites. Also, Tao's group²⁵

[†]Electronic supplementary information (ESI) available. See DOI: 10.1039/d1pr02347k

[‡]These authors contributed equally to this work.

Nanoscale Paper

reported Mn^{4+} rich Mg_2MnO_4 with remarkable discharge capacity and structural stability in aqueous batteries.

In addition to the above two strategies, tuning the spinel phase evolution process during cycling is another pathway to achieve high electrode performances. For example, Liu et al. 18 reported a significant electro-activation reaction in spinel ZnV₂O₄ with self-adaptive adjustment of the lattice structure, which guarantees outstanding electrochemical performance. Luo's group¹⁹ proposed that the formation of a new phase from order to disorder during cycling is responsible for the remarkable electrode performance of the spinel MgV2O4 cathode in AZIB. Lu et al.26 reported a rapid in situ transformation of V2O5 atomic layers into Zn3V2O7(OH)2·2H2O clusters with a high concentration of reactive sites for H⁺ and Zn²⁺ storage. Tang et al.27 presented the electrochemically induced formation of the disorder/order structure in FeVO4 spinel to improve the structural stability during Mg²⁺ storage. Although the above reports illustrate the significance of structure evolution in activating the capacity delivery of spinel hosts, their viewpoints and explanations are controversial. Thus, nowadays, research studies on structure evolution and energy storage behaviors of spinel host materials in aqueous batteries are far from clear.

Herein, for the first time, we provide the structure evolution and energy storage mechanism of spinel-type $\rm Zn_3V_3O_8$ in mild aqueous Zn-ion batteries. We find that the capacity of the $\rm Zn_3V_3O_8$ electrode can be effectively activated under high-voltage scanning in 3 M $\rm Zn(CF_3SO_3)_2$ electrolyte, and the structure evolution from bulk to nanocrystalline spinel is responsible for this capacity activation process. A proton and $\rm Zn^{2^+}$ cointercalation mechanism with a certain amount of water is illustrated for energy storage in this nanocrystalline spinel host, featuring a pseudo-capacitive intercalation behavior with superior diffusion kinetics. Consequently, the $\rm Zn_3V_3O_8$ spinel presents enhanced capacity and excellent cycling performance.

Experimental

Synthesis of Zn₃V₃O₈

The $\rm Zn_3V_3O_8$ sample was synthesized via a traditional solid-state method. Zinc acetate and vanadium oxide were added to the mortar as a mole ratio of $\rm Zn:V=1.05:1$. After homogeneous mixing for about half an hour, the sample was preheated to 500 °C for 3 h and then heated to 800 °C for 8 h in an Ar atmosphere. The heating rate was ~ 5 °C min⁻¹.

Materials characterization

The X-ray diffraction (XRD) patterns were obtained with a Bruker D8-Advance diffractometer using Cu-K α radiation (λ = 1.5406 Å), and the structure Rietveld refinement was performed using Fullprof. The size and morphology of the as-prepared Zn₃V₃O₈ were observed using a scanning electron microscope (SEM, ZEISS SUPRA55, Carl Zeiss) and a field emission transmission electron microscope (TEM, JEM-3200FS, JEOL). The elemental composition of the samples is characterized by

inductively coupled plasma-optical emission spectroscopy (ICP-OES, JY2000-2). The chemical states were evaluated by X-ray photoelectron spectroscopy (XPS, Thermo Fisher ESCALAB 250Xi).

Electrochemical tests

The powder of active materials was mixed with acetylene black and polyvinylidene fluoride (PVDF) with a weight ratio of 7:2:1 in N-methyl pyrrolidone (NMP) solvent. The mixture was stirred to form a homogeneous slurry, which was then pasted on a Ti foil and dried in a vacuum oven at 110 °C for 12 h. Zn metal was used as the anode and paired with cathode materials to fabricate a 2032 coin-type coin cell. The glass fiber served as the separator and the aqueous Zn(CF₃SO₃)₂ solution (1 M/2 M/3 M) as the electrolyte. All the coin cells were assembled under an ambient environment. The galvanostatic charge/discharge tests were applied using a battery test system (Neware Battery Cycler, Shenzhen, China). Cyclic Voltammetry (CV) was measured using a CH instrument electrochemical workstation. For comparison, the galvanostatic charge/discharge and CV were tested in different cut-off voltages (0.4-1.4 V, 0.4-1.7 V, and 0.4-2.0 V). The Galvanostatic Intermittent Titration Technique (GITT) was tested using a MACCOR Model MC-16 battery system with 10 minute discharging/charging and 30 minute resting.

Results and discussion

Material characterization

The spinel-type $\rm Zn_3V_3O_8$ product was synthesized by a traditional solid-state reaction between zinc acetate and vanadium oxide. The ICP-OES result indicates that the molar ratio of Zn/V in the product is ~1.11 (Table S1†). Fig. 1a shows the XRD pattern of the product, which can be well indexed to the $\rm Zn_3V_3O_8$ standard spinel card (space group of $\rm \it Fd\bar{\it 3m}$, PDF#31-1477). Furthermore, the Rietveld refinement is conducted using Fullprof, showing a great fit between the observed and calculated patterns ($\rm \it R_{wp}=6.73\%$). The corresponding atomic occupancies (Occ.) of Zn, V, and O in the spinel-type product are shown in Fig. 1b, and the corresponding crystal structure is shown in Fig. 1c, in which the Occ. of Zn in 8a and 16d sites are 1.03 and 0.282, Occ. of V in the 16d site is 0.718, and Occ. of O in the 32e site is 1.05, respectively.

The irregular micro-morphologies of $Zn_3V_3O_8$ are presented in Fig. S1 and S2.† It can be seen that the Zn, V, and O elements are uniformly distributed throughout the whole particle. The high-resolution transmission electron microscopy (HRTEM) is further applied to investigate the crystal structure of $Zn_3V_3O_8$ (Fig. 1d). Two well-resolved lattice fringes are observed, with an interlayer spacing of d_{111} = 0.484 nm and d_{220} = 0.296 nm, respectively, and the corresponding diffraction pattern is also consistent with the HRTEM results. Furthermore, the existence of Zn and mixed chemical valences

Paper

Zn 2p Observed (311)Zn 2p_{3/2} a Calculated Difference Intensity (a.u.) Fd-3m Zn 2p1/2 Zn₃V₃O₈ 1050 1040 1030 1020 Binding energy (eV) $d_{(111)} = 0.484 \text{ nm}$ V 2p_{3/2} f V 2p 20 40 60 80 100 120 2Theta (degree) V 2p_{1/2} b Intensity (a.u.) Wyckoff X Y \mathbf{Z} Atom Occ. position Satellite 0 Zn1 0 1.03 V 16d 0.625 0.625 0.625 0.718 16d 0.625 7n20.625 0.625 0.282 10 nm

Fig. 1 Material characterization of spinel-type $Zn_3V_3O_8$, (a) XRD refinement result of $Zn_3V_3O_8$ powder using Fullprof, (b) the atomic occupation of Zn, V, and O elements, (c) crystal structure, and (d) HRTEM morphology and diffraction pattern. XPS analysis of (e) Zn 2p and (f) V 2p peaks in Zn₃V₃O₈ powder.

of V^{3+} and V^{4+} in $Zn_3V_3O_8$ is depicted by the XPS results in Fig. 1e and f.

0.375

0.375

0.375

1.05

Electrochemical performance

O

32e

To evaluate the electrochemical performance of Zn₃V₃O₈, cointype Zn/Zn₃V₃O₈ cells are assembled, in which the Zn plate works as the anode, Zn₃V₃O₈ as the cathode, and the aqueous Zn(CF₃SO₃)₂ solution as the electrolyte. On tuning the Zn (CF₃SO₃)₂ concentration in the electrolyte and cell voltage ranges an optimized electrode performance can be achieved, as shown in Fig. S3.† It can be seen that the best cycling performance is achieved in the cell voltage range of 0.4-1.7 V in the concentrated electrolyte. Higher or lower cut-off voltages (2.0 V or 1.4 V) are inferior to capacity release, mainly due to the uncontrolled structure collapse and the insufficient redox reaction, respectively. All cycling profiles follow the same character, i.e., the discharge capacity increases rapidly to a peak value in initial cycles, then declines slowly in the following cycles. The inevitable capacity activation process indicates a structure evolution process in initial cycles, which will be depicted in the later part. Fig. 2a shows the cyclic voltammogram (CV) curves of the Zn/Zn₃V₃O₈ cell in the initial 5 cycles with a low scanning rate of ~ 0.1 mV s⁻¹. It can be observed that a towering oxidation peak is located at around 1.61 V in the 1st cycle, mainly due to facile Zn²⁺ extraction from the pristine Zn₃V₃O₈ electrode. After the 1st cycle, two pairs of redox peaks are observed located at 0.90/0.98 V and 0.56/0.72 V, respectively. Meanwhile, the redox current values increase

gradually upon cycling, which corresponds well to the capacity activation in the initial cycles.

Binding energy (eV)

Fig. 2b and c show the rate performance of Zn₃V₃O₈ after the initial capacity activation process (pre-cycling 20 cycles at 500 mA g⁻¹), as well as the galvanostatic charge/discharge (GCD) profiles at various rate currents. The results show discharge capacities of 294, 289, 275, 260, 245, and 229 mA h g^{-1} , at increasing rate currents of 100, 200, 500, 1000, 1500, and 2000 mA g⁻¹, respectively. Furthermore, the cycling performances of Zn/Zn₃V₃O₈ cells at rate currents of 500 mA g⁻¹ and 2000 mA g^{-1} are also provided in Fig. 2d and e. When operated at a current of 500 mA g-1, the discharge capacity first increases to 272 mA h g⁻¹ in the initial 37 cycles (capacity activation, as pointed by the arrow), and then decreases slowly to 200 mA h g^{-1} from 37 to 400 cycles, with a high capacity retention of \sim 73.8%. When tested at a current of 2000 mA g⁻¹, the discharge capacity first rises to 231 mA h g⁻¹ in the initial 114 cycles (capacity activation, as pointed by the arrow), then decreases slowly to 170 mA h g⁻¹ from 114 to 1200 cycles, with a high capacity retention of ~74.6%. The capacity, rate, and cycling performances of the Zn₃V₃O₈ cathode are among the best-reported electrode performances of spinel-type host materials (Table S2†).

Electrode/electrolyte interfacial reaction during cycling

Revealing the electrode reaction mechanism is vital for understanding the charge storage mechanism and the correlated electrode performances of Zn₃V₃O₈. Fig. 3a presents the XRD patterns of the pristine Zn₃V₃O₈ electrode, the electrode Nanoscale Paper

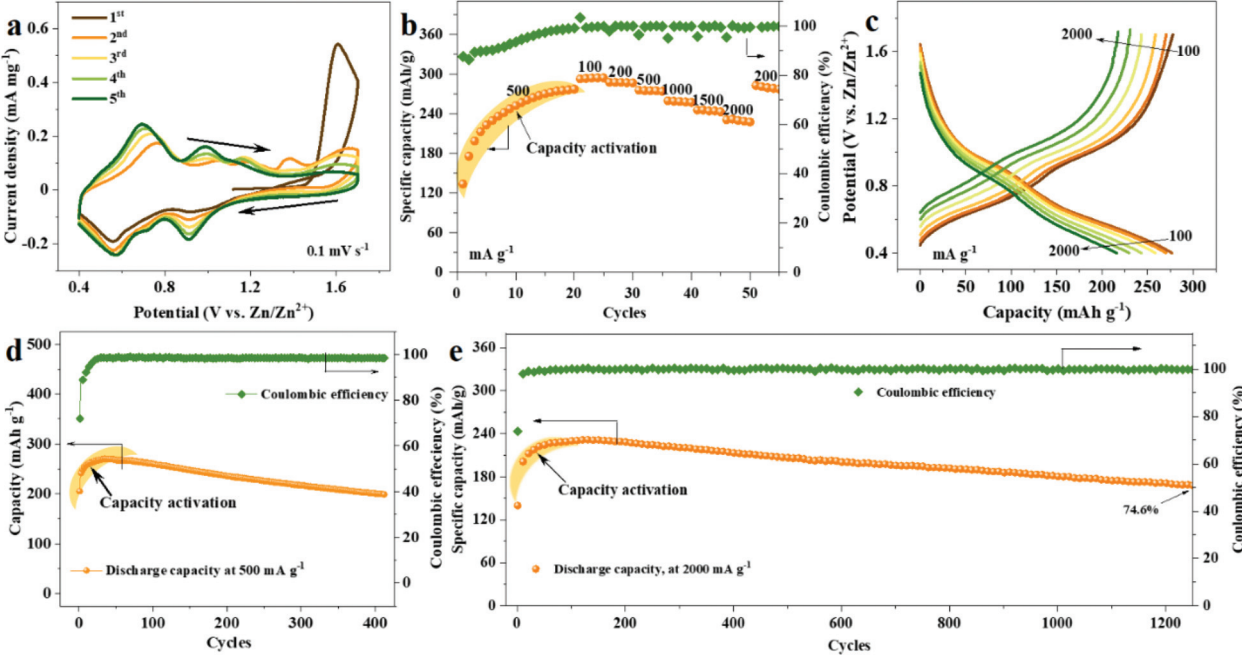


Fig. 2 Electrode performance of the $Zn_3V_3O_8$ electrode. (a) CV curves of the $Zn/Zn_3V_3O_8$ cell at 0.1 mV s⁻¹ in the cell voltage range of 0.4–1.7 V, in 3 M $Zn(CF_3SO_3)_2$ electrolyte. (b) Rate performances of the $Zn_3V_3O_8$ electrode in 3 M $Zn(CF_3SO_3)_2$ electrolyte, and (c) corresponding GCD curves in different rate currents. (d and e) Cycling performance at ~500 mA g^{-1} for over 400 cycles, and at ~2000 mA g^{-1} for over 1200 cycles.

immersed in the electrolyte for 12 h, and the electrodes at charged/discharged states in 1st, 2nd, and 5th cycles. The corresponding SEM morphologies are shown in Fig. 3b-i. After being immersed in 3 M Zn(CF₃SO₃)₂ electrolyte for 12 h, some nano-sheet by-products occur on the electrode surface, indicating a spontaneous side reaction (Fig. 3c). This by-product is also observed in other electrodes, including the charged electrode in the 1st cycle (Fig. 3d), and the discharged electrodes in the 1st, 2nd, and 5th cycle (Fig. 3e, g and i). Note that the byproducts in the 1st cycle may result from the immersion (Fig. 3b) instead of the charging process, which can be corroborated by the irregular electrochemical reactions in CV profiles (Fig. 2a). A sharp peak at $2\theta = 12.50^{\circ}$ refers to this byproduct (Fig. 3a and S7†), which is proved to be the characteristic peak of zinc hydroxide vanadium oxide hydrate $(Zn_3(OH)_2(V_2O_7)(H_2O)_2$, ZOVH, PDF#87-0417, hexagonal, $P\bar{3}m1$ (164)). The generation of ZOVH is further confirmed by TEM results (Fig. 3j and k), in which the Zn, O, and V elements are uniformly distributed, while no S and F elements are observed.

The crystal structure of ZOVH is presented in Fig. 3l. Since the formation of ZOVH needs a certain amount of OH^- and $V_2O_7^{\ 4^-}$ ions, which can't be directly obtained from the original $Zn(CF_3SO_3)_2$ electrolyte, there must be a spontaneous reaction between the electrolyte and electrode in immersing. Some H^+ ions from H_2O may insert into the electrode, leaving some OH^- ions on the electrode surface, and some $V_2O_7^{\ 4^-}$ ions are released from $Zn_3V_3O_8$. Then, the emerged OH^- and $V_2O_7^{\ 4^-}$ ions react with the Zn^{2^+} ions in the electrolyte, generating ZOVH deposits on the electrode surface, and the reaction occurs as given in formula (1):

$$3Zn^{2+} + 2OH^{-} + V_2O_7^{4-} + 2H_2O \rightarrow Zn_3(OH)_2(V_2O_7)(H_2O)_2$$
 (1)

For the electrode at charged states in the 1st cycle, the intensity of ZOVH remains unchanged, and the Zn/V ratio in the electrode (ZOVH on the electrode surface is removed by diluted H₂SO₄) decreases to 0.39 (obtained from the ICP results, Fig. S5†). This result indicates that a certain amount of Zn²⁺ is extracted from the electrode during the 1st charging process. Furthermore, the amount of ZOVH increases dramatically after the 1st discharge process (at 0.4 V) (Fig. 3a and e), demonstrating that plenty of protons are inserted into the electrode and more V2O74- ions are released from the electrode during discharge. In subsequent cycles, the ZOVH generates/ disappears reversibly (Fig. 3f-i), indicating a reversible proton intercalation/extraction during the discharge/charge processes. Besides, the characteristic peaks of Zn₃V₃O₈ weaken and disappear after the 1st cycle (Fig. 3a), demonstrating that the spinel phase of Zn₃V₃O₈ converts gradually to a short-range ordered spinel phase upon cycling.

During cycling, the ZOVH generates/disappears reversibly in the $2^{\rm nd}$ and $5^{\rm th}$ cycles. The ZOVH formation indicates that the extraction of $V_2O_7^{\ 4^-}$ ions and the proton insertion occur simultaneously upon discharge. So, we wonder where the extracted $V_2O_7^{\ 4^-}$ ions go when they are recharged to 1.7 V. Assuming that there exist three kinds of reactions for $V_2O_7^{\ 4^-}$ ions upon charging: (i) *in situ* depositing on the $Zn_3V_3O_8$ electrode, (ii) dissolving into the electrolyte, and (iii) moving forward to the Zn anode and forming ZOVH deposits upon cycling. Fig. S6† shows the evaluation of the variations of V

Paper Nanoscale

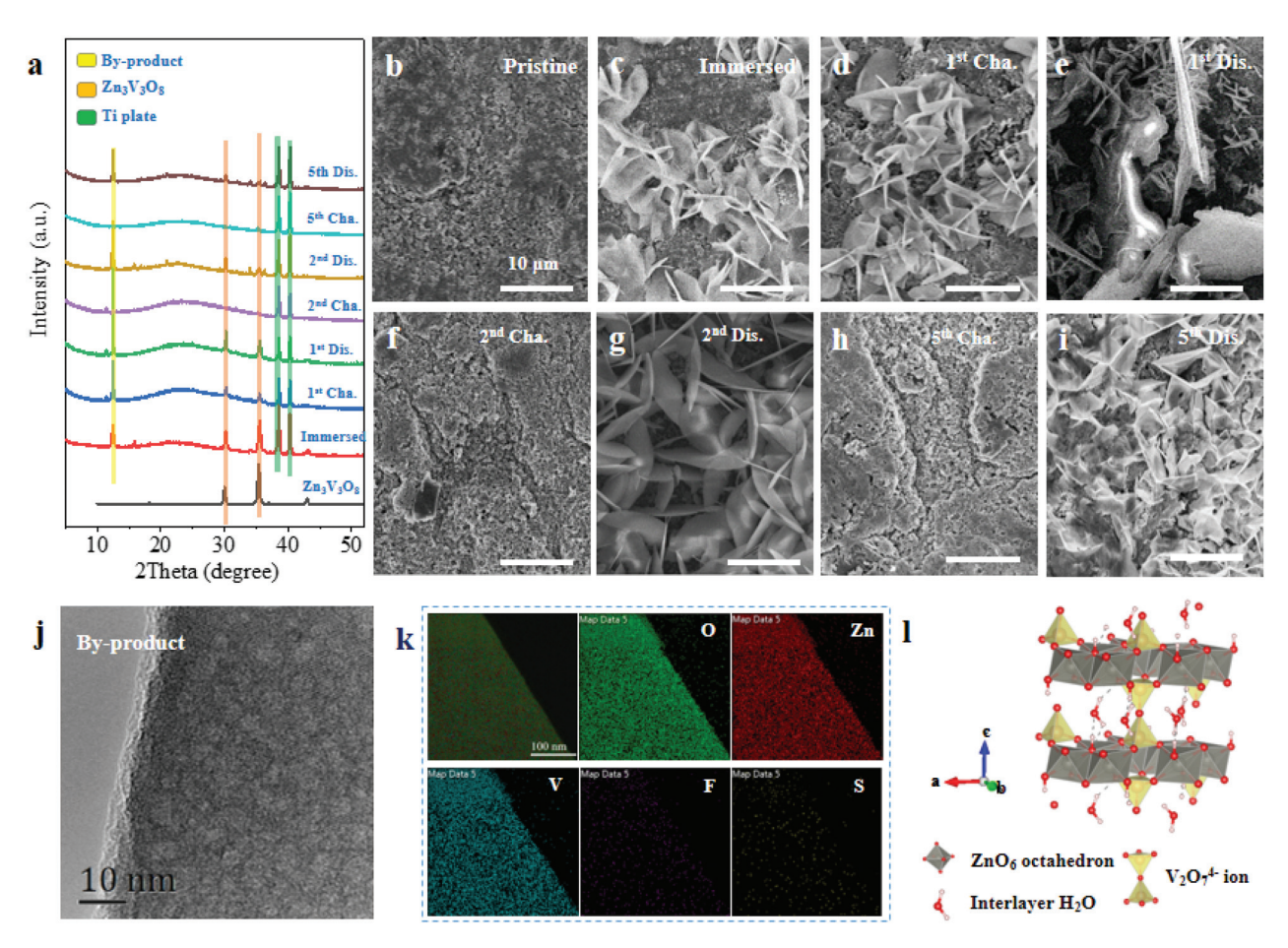


Fig. 3 Electrode reactions of $Zn_3V_3O_8$ in 3 M $Zn(CF_3SO_3)_2$ electrolyte. (a) XRD patterns and corresponding SEM morphologies of the $Zn_3V_3O_8$ electrode at different states, (b) pristine, (c) immersed, (d) charged and (e) discharged in the 1st cycle, (f) charged and (g) discharged in the 2nd cycle, and (h) charged and (i) discharged in the 5th cycle. (j) TEM morphology of $Zn_3V_3O_8$, (k) EDS-mapping of O, Zn, V, F, and S elements, (l) schematic illustration of the crystal structure of $Zn_3(OH)_2(V_2O_7)$ ($H_2O)_2$.

concentrations (using ICP-OES results) in electrolytes (collected in coin cells) in 100 cycles, which shows no free $V_2O_7^{\ 4-}$ ions in the electrolytes. Also, the XRD and SEM results of the Zn plate after cycled in the Zn/Zn₃V₃O₈ cell (Fig. S7 and S8†) are characterized, showing no characteristic peaks of ZOVH or enrichment of V elements existing on the Zn anode. Thus, the $V_2O_7^{\ 4-}$ ions dissolved upon charging are *in situ* deposited on the pristine Zn₃V₃O₈ electrode and form short-range ordered V-based deposits. Therefore, in this part, we reveal a spontaneous interfacial reaction between Zn₃V₃O₈ and aqueous electrolytes, *i.e.*, the reversible intercalation/extraction of protons and the formation/disappearance of ZOVH during cycling.

Structure evolution of Zn₃V₃O₈ during cycling

The HRTEM characterization studies are applied to reveal this structure evolution of $Zn_3V_3O_8$ upon cycling (Fig. 4). Before the HRTEM characterization studies, the ZOVH by-product on the electrode is pre-removed using dilute sulfuric acid. The spinel-type structure of $Zn_3V_3O_8$ remains unchanged after immersing in the electrolyte for 12 h (Fig. S9†), indicating no structure

evolution upon immersing. After being charged to 1.7 V in the $1^{\rm st}$ cycle, the characteristic XRD peaks of $Zn_3V_3O_8$ (2theta = 30.1° and 35.5°) remain stable (Fig. 3a), but with much-lowered intensities, the structural transformation to a short-range ordered spinel-type phase is illustrated. This spinel-type structure can be further confirmed by the HRTEM results in Fig. 4a, which shows clear lattice fringes of the (311) planes with a lattice spacing of $\sim\!0.263$ nm. When discharged to 0.4 V in the $1^{\rm st}$ cycle (Fig. 4b), the characteristic XRD peaks of $Zn_3V_3O_8$ are re-enhanced, and the diffraction pattern features an interlayer spacing of $\sim\!0.496$ nm of the (111) planes.

When it comes to the 2^{nd} cycle, the characteristic XRD peaks of $Zn_3V_3O_8$ spinel disappeared at the charged state and re-emerged at the discharged state (Fig. 3a). At the charged state, some lattice fringes of the (311) planes are observed in localized areas with a layer spacing of ~ 0.258 nm, as verified by HRTEM results and diffraction patterns in Fig. 4c. However, at the discharged state (Fig. 4d), a diffraction ring is observed with a lattice spacing of ~ 0.273 nm of the (220) plane, indicating a short-range ordered Zn–V–O spinel. Thus, a structure evolution from bulk to nanocrystalline spinel is obtained in

Nanoscale

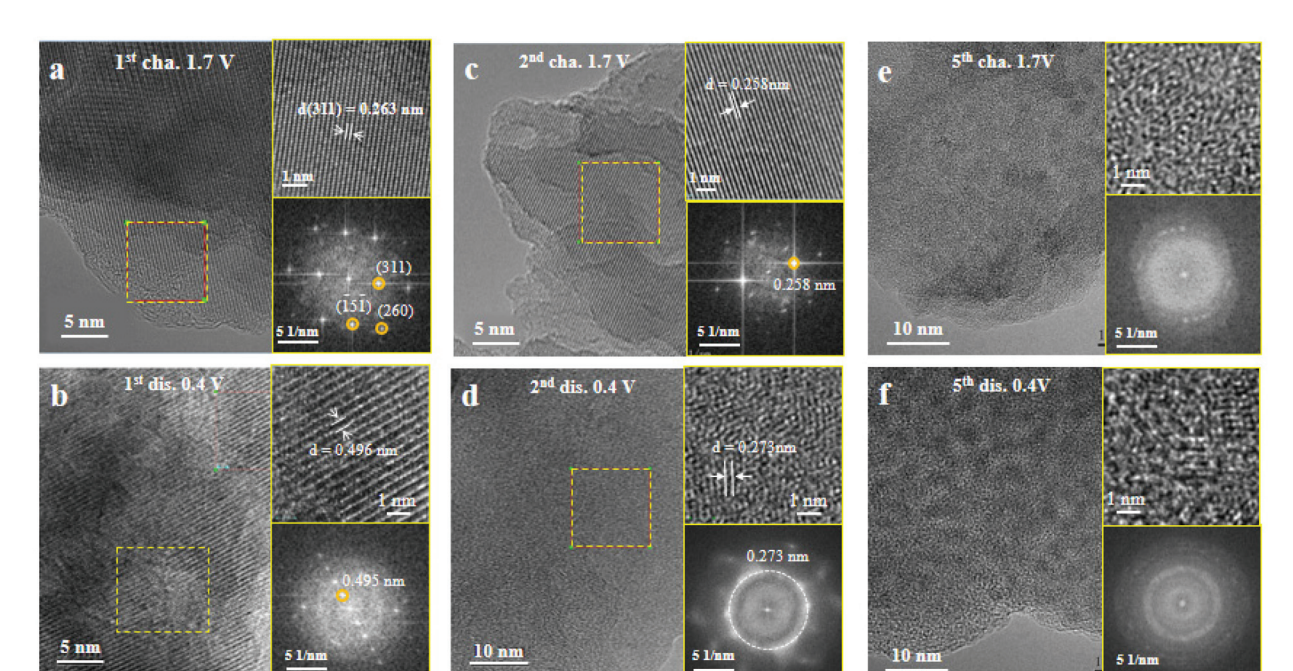


Fig. 4 Electrochemical structure evolution process of $Zn_3V_3O_8$ spinel. HRTEM analysis of the $Zn_3V_3O_8$ electrode at (a) the charged state (1.7 V) of the 1st cycle, (b) the discharged state (0.4 V) of the 2nd cycle, (c) the charged state (1.7 V) of the 2nd cycle, (d) the discharged state (0.4 V) of the 5th cycle, (e) the charged state (1.7 V) of the 5th cycle, (f) the discharged state (0.4 V) of the 5th cycle.

the 2^{nd} cycle. Subsequently, in the 5^{th} cycle, the characteristic XRD peaks of Zn–V–O spinel can still be observed for electrodes at the discharged state (Fig. 3a). The diffraction rings are observed in both the charged and discharged electrodes, as illustrated in Fig. 4e and f, indicating a stabilized nanocrystalline spinel. Besides, accompanying the structure evolution, the Zn/V ratio in the charged electrode decreases from 0.39 (in the 1^{st} cycle) to 0.11 (in the 10^{th} cycle) (Fig. S5†), indicating a continuous Zn^{2+} extraction from the lattice framework of $Zn_3V_3O_8$ during cycling, which may be responsible for the structure evolution. Thus, in this part, the structural evolution of $Zn_3V_3O_8$ from spinel to nanocrystalline Zn–V–O spinel is revealed upon cycling, which plays a vital role in activating the capacity of spinel-type $Zn_3V_3O_8$ in aqueous Zn-ion batteries.

In addition to the structure evolution, the XPS analyses are further applied to investigate the energy storage behavior in nanocrystalline Zn-V-O spinel (in the 5th cycle, a current of \sim 200 mA g⁻¹). Fig. 5a and d show the XPS analyses of O 1s peaks at the charged and discharged states, respectively. We observe that the relative intensities of H-O-H and V-O-H peaks are enhanced greatly after discharge, which illustrates the successful intercalation of H₂O and H⁺. As reported in previous reports, the co-intercalation of H2O benefits the diffusion kinetics of carrier ions. 28-30 Fig. 5b and e show the XPS analyses of Zn 2p peaks of amorphous Zn₃V₃O₈ at the charged and discharged states, respectively. The relative intensity of Zn 2p peaks is also enhanced slightly after discharge, illustrating the successful Zn²⁺ intercalation. The Zn²⁺ intercalation can also be confirmed by the TEM-mapping results shown in Fig. S10,† in which an obvious Zn enrichment is observed in the discharged $Zn_3V_3O_8$. Besides, the chemical valence of V in the amorphous Zn–V–O compound is also reduced upon discharge (Fig. 5c and f). Based on the above results, we conclude a H^+/Zn^{2+} co-intercalation with a certain amount of H_2O to dominate the capacity of $Zn_3V_3O_8$ during cycling, similar to the vanadium oxides in previous works. $^{31-33}$

Discussions

As discussed above, the structure evolution is significant for activating the capacity delivery of $Zn_3V_3O_8$ spinel in aqueous batteries. Fig. 6 presents the schematic illustration of the structure evolution mechanism of the $Zn_3V_3O_8$ spinel during cycling. Two types of reactions occur during cycling, *i.e.*, the interfacial reaction and electrode reaction. The interfacial reaction refers to the reversible formation/disappearance of ZOVH on the electrode surface during cycling, and the electrode reaction refers to the electrochemical structure evolution of $Zn_3V_3O_8$, and the correlated H^+/Zn^{2+} intercalations. $Zn_3P_3O_8$

When immersed in 3 M $Zn(CF_3SO_3)_2$ electrolyte, some spontaneous reactions occur, including a H^+ insertion, $V_2O_7^{\ 4-}$ dissolution, and subsequent formation of ZOVH by-products. During the 1^{st} charging process, only some Zn^{2+} ions are extracted, leaving the $Zn_3V_3O_8$ spinel framework with less Zn^{2+} . Then, during the subsequent discharging process, H^+/Zn^{2+} ions are re-inserted into the spinel framework. In the 2^{nd} charging/discharging process, there exists a reversible H^+/Zn^{2+} co-intercalation in the short-range ordered Zn-V-O spinel. After several cycles under the optimized test conditions, the

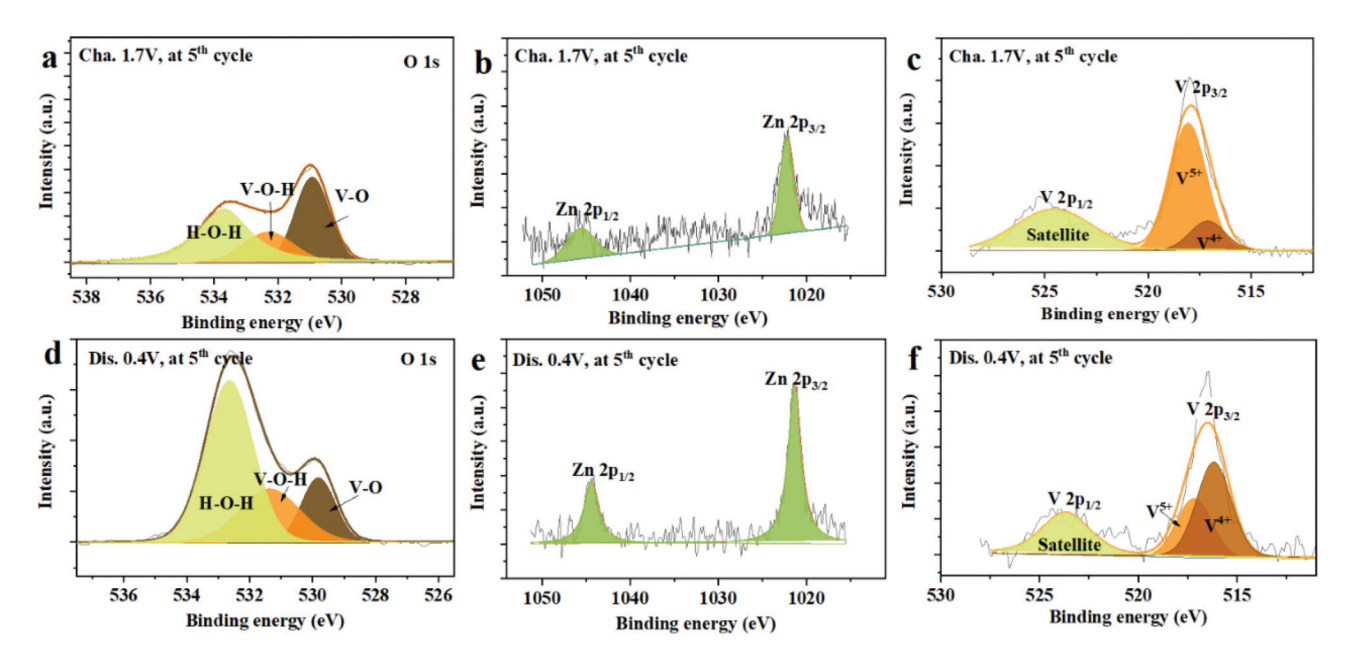


Fig. 5 Synthetic H^+/Zn^{2+} intercalation mechanism of the converted amorphous Zn-V-O compound. XPS analysis of (a) O 1s, (b) Zn 2p, and (c) V 2p spectra of the electrode at the charged state in the 5th cycle. XPS analysis of (d) O 1s, (e) Zn 2p, and (f) V 2p spectra of the electrode at the discharged state in the 5th cycle.

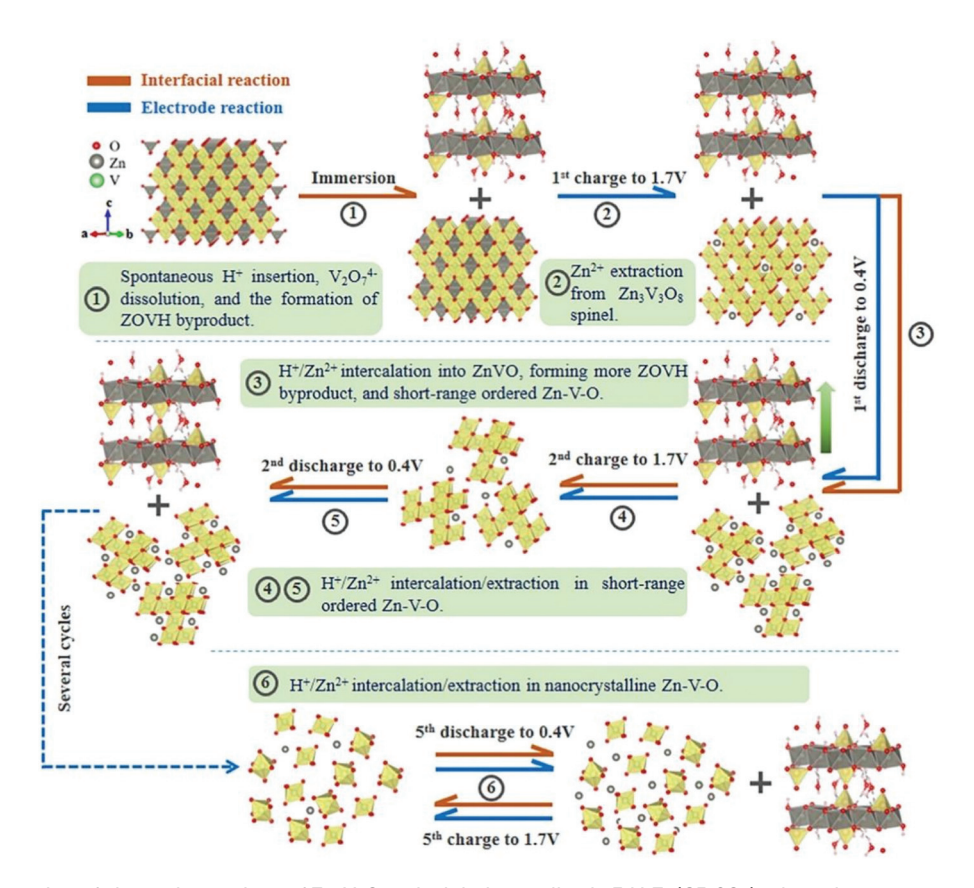


Fig. 6 Schematic illustration of electrode reactions of $Zn_3V_3O_8$ spinel during cycling in 3 M $Zn(CF_3SO_3)_2$ electrolyte.

Nanoscale Paper

 $\rm Zn_3V_3O_8$ completely converts to the nanocrystalline Zn-V-O spinel, and H⁺ and $\rm Zn^{2+}$ co-intercalation dominates the electrode capacity. It can be concluded that the nanocrystalline spinel is beneficial for capacity release.

We notice that aqueous electrolyte is significant for activating the "spinel to amorphous" phase conversions. When measured in the non-aqueous electrolyte, i.e., 0.3 M Zn (CF₃SO₃)₂ in dimethyl sulfoxide (DMSO), the bulk spinel framework of Zn₃V₃O₈ remains well after cycles (Fig. S11†), indicating that the "bulk to nanocrystalline" structure evolution is depressed in non-aqueous electrolytes. As a consequence, the reversible capacity in the non-aqueous electrolyte is very low (21 mA h g^{-1} at a current of 200 mA g^{-1}) (Fig. S12†). Such results also demonstrate that the nanocrystalline structure is vital for capacity activation. Benefiting from the "bulk to nanocrystalline" structure evolution, the superior reaction kinetics of the Zn₃V₃O₈ electrode is achieved. To illustrate the reaction kinetics of the electrodes, CV curves at different scanning rates, and corresponding calculations for $\log(i_p) - \log(\nu)$ curves are presented in Fig. S13, \dagger where i_p represents the current density values of redox peaks (mA mg⁻¹), and ν is the scan rate (mV s⁻¹).^{34,35} The calculated b values for O₁, O₂, R₁, and R₂ peaks are 0.836, 0.965, 0.869, and 0.905, respectively, indicating a pseudo-capacitive diffusion character for proton and Zn2+ insertion/extraction upon cycling. The nanocrystalline structure may have shortened diffusion channels for Zn²⁺, which contribute to the polarization alleviation and the rate performance improvement. The galvanostatic intermittent titration technique (GITT) results in Fig. S14† presents a high average diffusion coefficient of $\sim 7.78 \times 10^{-10}$ cm² s⁻¹, which is at a high level for V-based cathode materials in aqueous Znion batteries (Table S3†).

Conclusions

In this work, we synthesize a spinel-type $\rm Zn_3V_3O_8$ $\it via$ a simple solid-state reaction method. By tuning $\rm Zn(CF_3SO_3)_2$ concentrations in electrolytes and cell voltage ranges, an optimized electrode performance is achieved with a capacity activation process. We reveal a "bulk to nanocrystalline" structure evolution in $\rm Zn_3V_3O_8$ spinel for the capacity activation and propose a proton and $\rm Zn^{2+}$ co-intercalation mechanism for energy storage behavior in this nanocrystalline $\rm Zn\text{-}V\text{-}O$ spinel. The nanocrystalline $\rm Zn\text{-}V\text{-}O$ spinel presents a pseudo-capacitive diffusion character with excellent diffusion kinetics, which enables superior electrode performance. This work provides a new viewpoint of the charge storage mechanism in spinel-type host materials, which benefits the design and development of next-generation batteries.

Conflicts of interest

There are no conflicts to declare.

Acknowledgements

This work is financially supported by the Stable Support Funding for Universities in Shenzhen (No. GXWD20201231165807007 and 20200807111854001).

References

- 1 R. Qin, Y. Wang, Q. Zhao, K. Yang and F. Pan, Chin. J. Struct. Chem., 2020, 39, 605–614.
- 2 R. Qin, Y. Wang, M. Zhang, Y. Wang, S. Ding, A. Song, H. Yi, L. Yang, Y. Song, Y. Cui, J. Liu, Z. Wang, S. Li, Q. Zhao and F. Pan, *Nano Energy*, 2021, 80, 105478.
- 3 Q. Zhao, A. Song, S. Ding, R. Qin, Y. Cui, S. Li and F. Pan, *Adv. Mater.*, 2020, 32, 2002450.
- 4 Y. Cui, Q. Zhao, X. Wu, X. Chen, J. Yang, Y. Wang, R. Qin, S. Ding, Y. Song, J. Wu, K. Yang, Z. Wang, Z. Mei, Z. Song, H. Wu, Z. Jiang, G. Qian, L. Yang and F. Pan, *Angew. Chem.*, 2020, 59, 16594–16601.
- 5 B. Zhang, Z. Li, Q. Li, Z. Lin, J. Liu and F. Pan, *Chin. J. Struct. Chem.*, 2020, **39**, 11–21.
- 6 M. J. Park, H. Yaghoobnejad Asl and A. Manthiram, ACS Energy Lett., 2020, 5, 2367–2375.
- 7 Q. Zhao, A. Song, W. Zhao, R. Qin, S. Ding, X. Chen, Y. Song, L. Yang, H. Lin, S. Li and F. Pan, *Angew. Chem.*, 2021, 60, 4169–4174.
- 8 M. Liu, Q. Zhao, H. Liu, J. Yang, X. Chen, L. Yang, Y. Cui, W. Huang, W. Zhao, A. Song, Y. Wang, S. Ding, Y. Song, G. Qian, H. Chen and F. Pan, *Nano Energy*, 2019, **64**, 103942.
- 9 H. Yi, R. Qin, S. Ding, Y. Wang, S. Li, Q. Zhao and F. Pan, Adv. Funct. Mater., 2021, 31, 2006970.
- L. Ma, S. Chen, C. Long, X. Li, Y. Zhao, Z. Liu, Z. Huang,
 B. Dong, J. A. Zapien and C. Zhi, *Adv. Energy Mater.*, 2019,
 9, 1902446.
- 11 Z. Tie, L. Liu, S. Deng, D. Zhao and Z. Niu, *Angew. Chem.*, 2020, **59**, 4920–4924.
- 12 C. Strietzel, M. Sterby, H. Huang, M. Strømme, R. Emanuelsson and M. Sjödin, *Angew. Chem.*, 2020, **59**, 9631–9638.
- 13 K. Liao, H. Wei, P. Shi, J. Fan, Q. Xu and Y. Min, *J. Mater. Chem. A*, 2020, **8**, 21163–21172.
- 14 J. Du, S. Gao, P. Shi, J. Fan, Q. Xu and Y. Min, J. Power Sources, 2020, 451, 227727.
- 15 R. Dai, Y. Zhang, J. Fan, Q. Xu and Y. Min, *ACS Sustainable Chem. Eng.*, 2020, **8**, 18636–18645.
- 16 S. Islam, M. H. Alfaruqi, D. Y. Putro, S. Park, S. Kim, S. Lee, M. S. Ahmed, V. Mathew, Y.-K. Sun, J.-Y. Hwang and J. Kim, *Adv. Sci.*, 2021, 8, 2002636.
- 17 N. Zhang, F. Cheng, Y. Liu, Q. Zhao, K. Lei, C. Chen, X. Liu and J. Chen, J. Am. Chem. Soc., 2016, 138, 12894– 12901.
- 18 Y. Liu, C. Li, J. Xu, M. Ou, C. Fang, S. Sun, Y. Qiu, J. Peng, G. Lu, Q. Li, J. Han and Y. Huang, *Nano Energy*, 2020, 67, 104211

Paper Nanoscale

- 19 W. Tang, B. Lan, C. Tang, O. An, L. Chen, W. Zhang, C. Zuo, S. Dong and P. Luo, ACS Sustainable Chem. Eng., 2020, 8, 3681-3688.
- 20 L. Yang, K. Yang, J. Zheng, K. Xu, K. Amine and F. Pan, Chem. Soc. Rev., 2020, 49, 4667-4680.
- 21 T. Liu, A. Dai, J. Lu, Y. Yuan, Y. Xiao, L. Yu, M. Li, J. Gim, L. Ma, J. Liu, C. Zhan, L. Li, J. Zheng, Y. Ren, T. Wu, R. Shahbazian-Yassar, J. Wen, F. Pan and K. Amine, Nat. Commun., 2019, 10, 4721.
- 22 J. Ji, H. Wan, B. Zhang, C. Wang, Y. Gan, Q. Tan, N. Wang, J. Yao, Z. Zheng, P. Liang, J. Zhang, H. Wang, L. Tao, Y. Wang, D. Chao and H. Wang, Adv. Energy Mater., 2021, 11, 2003203.
- 23 C. Pan, R. Zhang, R. G. Nuzzo and A. A. Gewirth, Adv. Energy Mater., 2018, 8, 1800589.
- 24 C. Zuo, Z. Hu, R. Qi, J. Liu, Z. Li, J. Lu, C. Dong, K. Yang, W. Huang, C. Chen, Z. Song, S. Song, Y. Yu, J. Zheng and F. Pan, Adv. Energy Mater., 2020, 10, 2000363.
- 25 X. Yuan, T. Sun, S. Zheng, J. Bao, J. Liang and Z. Tao, J. Mater. Chem. A, 2020, 8, 22686-22693.
- 26 Y. Lu, T. Zhu, W. van den Bergh, M. Stefik and K. Huang, Angew. Chem., 2020, 59, 17004-17011.

- 27 C. Tang, F. Xiong, B. Lan, S. Tan, S. Dong, W. Zhang, C. Zuo, W. Tang, Q. An and P. Luo, Chem. Eng. J., 2020, 382, 123049.
- 28 Q. Zhao, L. Liu, J. Yin, J. Zheng, D. Zhang, J. Chen and L. A. Archer, Angew. Chem., 2020, 59, 3048-3052.
- 29 O. Zhao, S. Ding, A. Song, R. Oin and F. Pan, Chin. I. Struct. Chem., 2020, 39, 388-394.
- 30 Q. Zhao, X. Chen, Z. Wang, L. Yang, R. Qin, J. Yang, Y. Song, S. Ding, M. Weng, W. Huang, J. Liu, W. Zhao, G. Qian, K. Yang, Y. Cui, H. Chen and F. Pan, Small, 2019, **15**, 1904545.
- 31 X. Liu, H. Euchner, M. Zarrabeitia, X. Gao, G. A. Elia, A. Groß and S. Passerini, ACS Energy Lett., 2020, 5, 2979-2986.
- 32 Y. Dong, M. Jia, Y. Wang, J. Xu, Y. Liu, L. Jiao and N. Zhang, ACS Appl. Energy Mater., 2020, 3, 11183-11192.
- 33 Z. Li, S. Ganapathy, Y. Xu, Z. Zhou, M. Sarilar and M. Wagemaker, Adv. Energy Mater., 2019, 9, 1900237.
- 34 Z. Yao, Q. Wu, K. Chen, J. Liu and C. Li, Energy Environ. Sci., 2020, 13, 3149-3163.
- 35 Y. Cai, R. Chua, Z. Kou, H. Ren, D. Yuan, S. Huang, S. Kumar, V. Verma, P. Amonpattaratkit and M. Srinivasan, ACS Appl. Mater. Interfaces, 2020, 12, 36110-36118.